Measuring the degree of "nanotilization" of volcanic glasses: Understanding *syn*-eruptive processes recorded in melt inclusions

Danilo Di Genova [a,b,*], Alberto Caracciolo [c], Stephan Kolzenburg [d,e]

[a] *School of Earth Sciences, University of Bristol, Wills Memorial Building, Queens Road, Bristol BS8 1RJ, UK*
[b] *Institute of Non-Metallic Materials, Clausthal University of Technology, Zehntner Str. 2a, 38678 Clausthal-Zellerfeld, Germany*
[c] *Institute of Earth Sciences, University of Iceland, Sturlugata 7, 101 Reykjavík, Iceland*
[d] *Department of Earth and Planetary Sciences, McGill University, 3450 rue University, Montreal, QC, Canada H3A 2A7*
[e] *Department of Earth and Environmental Sciences, Ludwig-Maximilians-Universität München, Theresienstrasse 41/III, 80333 München, Germany*

ARTICLE INFO

ABSTRACT

Iron and water content substantially affect the physical properties of natural silicate melts and may, therefore, influence magmatic and volcanic processes such as crystallization, degassing, flow behaviour and eruptive style. Here we present Raman spectroscopic data for a set of synthetic and natural multicomponent glasses with varying iron oxidation state and water content. We systematically study the effect of different Raman excitation sources on the spectral response of both crystal free and magnetite nanolite bearing glasses spanning basaltic to calc- and per-alkaline rhyolitic compositions. Based on these data we document changes in Raman spectra resulting from the formation of nano-scale crystals. We show that the peak located at ~970 cm^{-1} is directly related to the presence of Fe_2O_3 dissolved in the quenched melt structure and that this feature is present regardless of the chemical composition of the sample and the Raman excitation source. We further show that a peak between 670 and 690 cm^{-1}, which is not related to any other spectral feature of the glass structure, reveals the presence of nanolites. Based on systematic spectral investigations of this feature, we present a new index that allows to identify if iron is present in the nanocrystalline state and/or bound in the glass structure. Since the melt structural and physical effects of the formation of nanolites can heavily affect the flow behaviour of melts and the eruptive style of volcanoes, the results presented in this study significantly broaden the application of Raman spectroscopy for investigations of nano-heterogeneity in synthetic and natural glasses.

We apply this method to study both the degree of nanolitization as well as the H_2O content and iron oxidation state of groundmass glasses as well as melt inclusions and glass embayments in explosive products from Pantelleria island (Italy). We observe that the process of nanotilization is not purely restricted to magnetite nanolites but that Raman spectroscopy may also identify the incipient crystalization of pyroxene and feldspar at sub-micron scale. The data document that nanolite formation correlates well with the observed intensity of the respective eruptions suggesting that structural changes in the melt, caused by incipient crystallization play an important role in defining the eruptive style of relatively low viscosity magmas.

1. Introduction

Magma transport plays a fundamental role in the evolution of planets (van Keken, 2003) and the activity and eruption style of volcanoes (Gonnermann and Manga, 2007). Its eruption on the Earth's surface can pose a significant threat to economic activities and human lives (Newhall et al., 2018). Silicate melt is, in most cases, the fundamental component of magma and its viscosity plays a key part in controlling magma mobilization and transport (Hammer et al., 1999; Petford, 2003;

Pistolesi et al., 2011; Zhang, 1999). The viscosity of a natural silicate melts can vary by several order of magnitude as function of chemical composition (X), temperature (T), and oxygen fugacity (fO_2) (Bouhifd et al., 2004; Hui and Zhang, 2007; Kolzenburg et al., 2018; Stabile et al., 2016; Webb et al., 2014). This dramatically affects the magmas transport dynamics and thus its eruptive behaviour. Changes in melt viscosity are the result of modifications in the structural interconnectivity of the melt and changes in the size of tetrahedra rings that are mostly driven by changes in X-T-fO_2 (Kubicki and Toplis, 2002; McMillan, 1984; Mysen, 1999; Sharma et al., 1981; Toplis et al., 1997). Therefore, understanding the X-T-fO_2 dependent structure-properties relationship represents a core challenge in advancing our knowledge of magmatic and volcanic processes and can inform conceptual and computational approaches to hazard forecasting.

---

* Corresponding author at: Institute of Non-Metallic Materials, Clausthal University of Technology, Zehntner Str. 2a, 38678 Clausthal-Zellerfeld, Germany

E-mail address: danilo.di.genova@tu-clausthal.de (D. Di Genova).

The structure of silicate melts consists of a three-dimensionally interconnected network of different units (Mysen and Richet, 2005 and reference therein). Tetrahedral units, the so-called Q^n species, are distinguished by the number (n) of bridging oxygens (BO), which ranges between 0 and 4, that connect Q^n species. These species are coordinated by network-former cations which, in magmatic melts, are dominantly Si^{+4}, Al^{3+}, and Fe^{3+}.

Iron is the most abundant 3d-transition element in volcanic systems and can be subjected to changes throughout magmatic and volcanic processes. The redox state of iron (ferrous Fe^{2+} and ferric Fe^{3+}) greatly affects its role in the melt structure and thus its properties as well as the stability of Fe-bearing phases (Bouhifd et al., 2004; Dingwell et al., 1988; Giordano et al., 2015; Liebske et al., 2003; Mysen et al., 1985; Wilke, 2005). The $Fe^{3+}/Fe_{tot.}$ ratio changes significantly with X-T-fO_2 conditions. Several studies have shown the effect of changing the redox state of iron on the physical properties of volcanic melts (Botcharnikov et al., 2005; Bouhifd et al., 2004; Di Genova et al., 2017c; Dingwell and Virgo, 1987; Kolzenburg et al., 2018; Liebske et al., 2003; Poe et al., 2012; Stabile et al., 2016; Toplis and Carroll, 1995).

Further, a recent study by Di Genova et al. (2017a), documented how the presence of magnetite nano-crystals, termed nanolites, can alter the structure and viscosity of volcanic melts. It was demonstrated that the formation of nanolites results in a viscosity increase of up to two orders of magnitude. It is also argued that iron oxides may provide nucleation sites for bubbles (Gardner and Denis, 2004; Pleše et al., 2018; Shea, 2017). Over the last few years, nanolites were also documented in products of explosive eruptions at basaltic and andesitic volcanoes such as Etna (Italy, Barone et al., 2016), Mount Ngauruhoe (New Zealand, Zellmer et al., 2016), Shinmoedake volcanoes (Japan, Mujin et al., 2017; Mujin and Nakamura, 2014) and the Menan Volcanic Complex (USA, Xu et al., 2017). The above summary of observations suggests that the precipitation of nanolites during magma ascent and decompression can play a crucial role in controlling the eruptive style.

Furthermore, the nano-heterogeneity of volcanic melts raises a fundamental question about our ability to model the viscosity of the melt fraction constituting the magma. Indeed, the parameterization of viscosity (e.g. Giordano et al., 2008; Hui and Zhang, 2007) often relies on melt chemistry measurements at a larger scale (i.e. microscale) than the nanocrystals and, thus, returning a seemingly homogenous bulk analysis of a heterogeneous material.

Raman spectroscopy has largely been used to infer the network connectivity of synthetic and volcanic melts and glasses (Ardia et al., 2014; Di Genova et al., 2017c; McMillan and Piriou, 1982; Mysen et al., 1982), estimate volatile content (Behrens et al., 2006; Di Genova et al., 2017b; Mercier et al., 2010; Morizet et al., 2013; Schiavi et al., 2018; Thomas, 2000), and approximate the $Fe^{3+}/Fe_{tot.}$ ratio and chemistry of volcanic glasses (Di Genova et al., 2016a, 2016b; Di Muro et al., 2009). However, while recent studies focused on the effect of nanolites on viscosity and estimation of water content, so far, no study has been presented to systematically characterize the degree of nano-*heterogeneity* of volcanic glasses.

Here, we expand the use of Raman spectroscopy to systematically study heterogeneities in volcanic products by measuring the degree of "*nanotilization*" of glasses over a large range of chemical composition. To this aim, we first carefully study the effect of the most common excitation sources for Raman spectroscopy on the spectral feature related to the presence of magnetite nanolites. We then introduce a new index termed *N#* (i.e. nanolite number) to constrain the degree of "*nanotilization*" calculated from Raman spectra of glasses. This new tool enables the user to infer the effect of nanoparticles on experimental results (Di Genova et al., 2017b; Di Muro et al., 2006a; Schiavi et al., 2018) and eruptive dynamics (Di Genova et al., 2017a; Mujin et al., 2017; Mujin and Nakamura, 2014). It further enables comparative studies of results obtained from different laboratories.

2. Methodology

2.1. Starting materials

Four iron-rich rhyolites (Fsp series, from Di Genova et al., 2016b) were used to investigate the effect of laser wavelength on Raman spectra of homogenous and nanolite-free glasses characterized by different iron oxidation state (Fe^{3+}/Fe_{tot} ratio ranging from 0.24 to 0.83). The effect of nanolites on Raman spectra was studied using six magnetite-nanolite-bearing glasses of different composition. Specifically, we selected three glasses from the calc-alkaline magma series: basaltic (KR3) and dacitic (HO2) glasses from Di Genova et al. (2017b) and a rhyolite (L, from Di Genova et al., 2017a). We further analysed three alkali-rich samples, namely a trachy-basalt (ETN3.8), trachyte (AMS4) and latite (FR3.8) from Di Genova et al. (2014a, 2014b). The Raman spectra acquired from these samples suggested that the mineral phase is magnetite (Di Genova et al., 2017b). Magnetic-hysteresis performed on the rhyolitic sample (L, Di Genova et al., 2017a) showed that the nanolite diameter ranges between ~5 nm to ~30 nm. We acknowledge that, according to Mujin et al. (2017), particles below ~30 nm can be classified as "ultrananolite" and that the term "nanolite" is suggested for describing those from 30 nm to 1 μm in width. In this study, we use the term "nanolite" for all samples because no information on the diameter of particles dispersed in our samples are available, except for sample L. Details of the experimental procedures to synthesise these samples, together with the techniques to estimate the iron oxidation state and water content, are reported in the respective studies. The samples used for application of the developed method to natural samples were collected from the basal vitrophyre of the Green Tuff ignimbrite (45–50 ka, Civetta et al., 1984) and Cuddia del Gallo cone (~6 ka, Mahood and Hildreth, 1986; Gioncada and Landi, 2010) on Pantelleria island (Italy), respectively.

The chemical compositions of all synthetic samples are reported in Table 1, while the chemistry of natural samples is reported in Table 2. All synthetic compositions are plotted in a TAS (total alkali versus silica) diagram in Fig. 1.

2.2. Raman spectroscopy

Raman spectra were acquired using a Thermo Scientific™ DXR™xi Raman Imaging Microscope at the University of Bristol, School of Earth Sciences. The instrument is equipped with three different lasers i) blue, 455 nm diode, ii) green, 532 nm doubled Nd:YVO4 DPSS and iii) red, 633 nm HeNe. Each laser is coupled with a single grating; the spectral resolution is ~2 cm^{-1}. Spectra collected with the blue laser (455 nm) were acquired using a 1200 lines*mm^{-1} grating. The green laser (532 nm) is coupled with a 900 lines*mm^{-1} grating, and the red laser (633 nm) is coupled with a 600 lines*mm^{-1} grating. It must be noted that only the green laser configuration allows for measurements from 50 to 4000 cm^{-1}.

Spectra of synthetic samples were acquired between 50 cm^{-1} and 1500 cm^{-1} using a high confocality setting with a 100× objective, 25 μm confocal pinhole, and a laser power between 3 and 6 mW measured on the sample surface in order to avoid oxidation of the sample (Di Genova et al., 2017b). All the spectra were acquired at ~5 μm of depth where the Raman signal was found to be at its optimum. In order to maximise the signal/noise ratio, the acquisition time and repetitions ranged between 8 and 15 s and 30–50 times, respectively. Different acquisition times were chosen to compensate for the differences in photon flux per pixel due to differences in the dispersion of employed gratings. Raman spectra of natural samples were collected between 100 cm^{-1} and 4000 cm^{-1} using the green laser, with an acquisition time of 15 s and 10 repetitions. Raman maps of the natural samples were produced using a linear magnetic stage coupled with optical encoders which allows maintaining the x-y-z position repeatability to within 10 nm. The DXR™xi Raman Imaging system is equipped with

Table 1
Chemical composition (in wt%) and $Fe^{3+}/Fe_{tot.}$ ratio of samples used in this study.

Sample	Composition	SiO_2	TiO_2	Al_2O_3	$FeO_{tot.}$	MnO	MgO	CaO	Na_2O	K_2O	H_2O	Fe^{3+}/Fe_{tot}	$N\#_{blue}$*	$N\#_{green}$*	$N\#_{red}$*
Fsp_1[a]	Iron-rich rhyolite	72.53	0.44	8.70	9.02	0.34	0.17	0.45	4.59	4.09	0.00	0.83	–	–	–
Fsp_4[a]	Iron-rich rhyolite	71.93	0.43	8.97	8.93	0.37	0.17	0.46	4.72	4.18	0.00	0.62	–	–	–
Fsp_7[a]	Iron-rich rhyolite	73.44	0.43	9.05	7.71	0.35	0.17	0.40	4.08	3.99	0.00	0.35	–	–	–
Fsp_9[a]	Iron-rich rhyolite	74.24	0.44	9.01	7.04	0.36	0.17	0.47	4.19	4.14	0.00	0.24	–	–	–
ETN3.8[b]	Trachybasalt	46.89	1.61	16.35	10.18	0.20	5.38	9.79	3.38	1.70	3.76	–	0.74	1.03	1.22
KR3[c]	Basalt	50.24	1.99	13.55	14.08	0.25	5.86	10.09	2.46	0.32	4.67	–	2.94	4.44	5.26
HO2[c]	Dacite	66.70	0.77	15.96	5.02	0.12	1.70	4.65	3.70	2.23	3.54	–	1.59	3.33	5.00
FR3.8[b]	Latite	54.69	0.77	17.41	6.35	0.17	2.14	5.20	4.30	4.32	3.76	0.41	2.22	3.45	5.26
AMS4[b]	Trachyte	59.67	0.53	18.69	4.08	0.14	1.22	0.60	4.07	7.91	4.78	–	0.87	1.28	1.89
L[d]	Iron-poor rhyolite	73.75	0.31	11.99	3.31	0.07	1.64	2.98	3.16	3.56	0.00	0.60	1.47	2.94	4.76

*Calculated nanolite number $N\#$ after Eq. 1 using different lasers.
[a] Di Genova et al. (2016a).
[b] Di Genova et al. (2014a).
[c] Di Genova et al. (2017b).
[d] Di Genova et al. (2017a).

an electron multiplied charge coupled device (EMCCD) used to amplify the signal without amplifying readout noise. This results in an extremely fast acquisition time (< 1 s) per 50 to 4000 cm^{-1} spectrum thus permitting to acquire thousands of spectra in a few minutes. This enables us to map relatively large areas (mm^2) in a satisfactory timeframe and, importantly, without heating and/or otherwise altering the sample.

All spectra were corrected for temperature and excitation line effects according to Long (1977). In order to subtract the spectra background, cubic splines were fit through intervals devoid of peaks in the silicate region (from 100 to ~200 and 1250 to 1500 cm^{-1}) and in the water region (2750–3100 and 3750–3900 cm^{-1}). The resulting spectra were normalised to the total area. All spectra were smoothed using Fourier transforms. The water content dissolved in melt inclusions was estimated using the procedure and pantelleritic standards described in Di Genova et al. (2017b).

2.3. Chemical analyses

Electron microprobe analyses of natural samples were performed using a Cameca SX-100 electron microprobe (School of Earth Sciences, University of Bristol, UK), equipped with 5 wavelength dispersive spectrometers and 1 energy dispersive. Analytical conditions were 4 nA beam current and 20 kV acceleration voltage. A defocused 10 μm beam was used for all elements to minimize the loss of volatile elements such as alkalis. Standards used were Amelia albite (Na, Si), Eifel Sanidine (Al, K), St. John's Island olivine (Mg), wollastonite (Ca), ilmenite (Ti, Fe), $BaSO_4$ (S), Durango apatite (P), halite (Cl), MnO (Mn), Cr_2O_3 (Cr) and data were reduced following the XPP routine.

3. Results

Raman spectra of synthetic glasses characterized by different $Fe^{3+}/Fe_{tot.}$ ratio (Fsp series, pantellerite) acquired using the blue, green, and red lasers are shown in Fig. 2a–d. Spectra from nanolite-bearing glasses with different chemical composition are reported in Fig. 3a–f. Chemical composition and $Fe^{3+}/Fe_{tot.}$ ratio of glasses are reported in Table 1.

For comparison, we also report Raman spectra of the most oxidized of the investigated iron-rich rhyolites (Fsp1 sample, $Fe^{3+}/Fe_{tot.} = 0.83$) collected using the three lasers in Fig. 2a. Overall, the signal/background ratio of the spectra changes with the excitation source. As showed in Fig. 2a, the spectra acquired with the red laser exhibit the lowest signal/background ratio, while spectra collected with the blue laser show the highest signal/background ratio.

After background subtraction and area normalization (Fig. 2b–d), excluding the sample with the lowest Fe_2O_3 content ($Fe^{3+}/Fe_{tot.} = 0.24$), the Raman spectra are dominated by the feature at ~970 cm^{-1}. The spectrum of the Fe^{3+}-poor sample ($Fe^{3+}/Fe_{tot.} = 0.24$) shows a peak at ~1040 cm^{-1}. These spectral signatures have been observed and studied extensively in spectra of simple and multicomponent systems collected with green lasers (Di Muro et al., 2009; Fox et al., 1982; Sharma et al., 1997; Virgo et al., 1983; Wang et al., 1993; Wang et al., 1995). The ~970 cm^{-1} contribution was assigned to an antisymmetric coupled mode of Fe^{3+} in four-fold coordination state, while the ~1040 cm^{-1} is characteristic of Fe^{2+} rich pantelleritic glasses (Di Genova et al., 2016a; Di Muro et al., 2009). The data presented here demonstrate that these observations hold true regardless of the excitation source employed to acquire the spectra (i.e. independent of laser wavelength).

Spectra collected from synthetic nanolite-bearing glasses are shown in Fig. 3a–f. The spectra show a broad resemblance to those of pure silicate glasses, but they possess distinct additional vibrational contributions located between 670 and 690 cm^{-1} and ~300 cm^{-1} that are not related to the glass structure. For pure volcanic glasses, depending on the SiO_2 content, the maximum Raman intensity is expected either at ~500 or ~1000 cm^{-1}, depending on the dominant structural contributor (Di Genova et al., 2015; Di Genova et al., 2016b; Di Muro et al., 2009; Mercier et al., 2009; Schiavi et al., 2018). Here, the main peak position occurs either at ~670 cm^{-1} for SiO_2-rich sample (rhyolite) or at ~690 cm^{-1} for SiO_2-poor samples (basalt). Based on data from the RRUFF database (Lafuente et al., 2015) and previous studies (Di Genova et al., 2017b; Di Muro et al., 2006a), this peak can be assigned to the presence of magnetite nanolites. This spectral feature is present in all spectra independent of the laser wavelength. However, we note that the intensity of this peak changes systematically as a function of the excitation
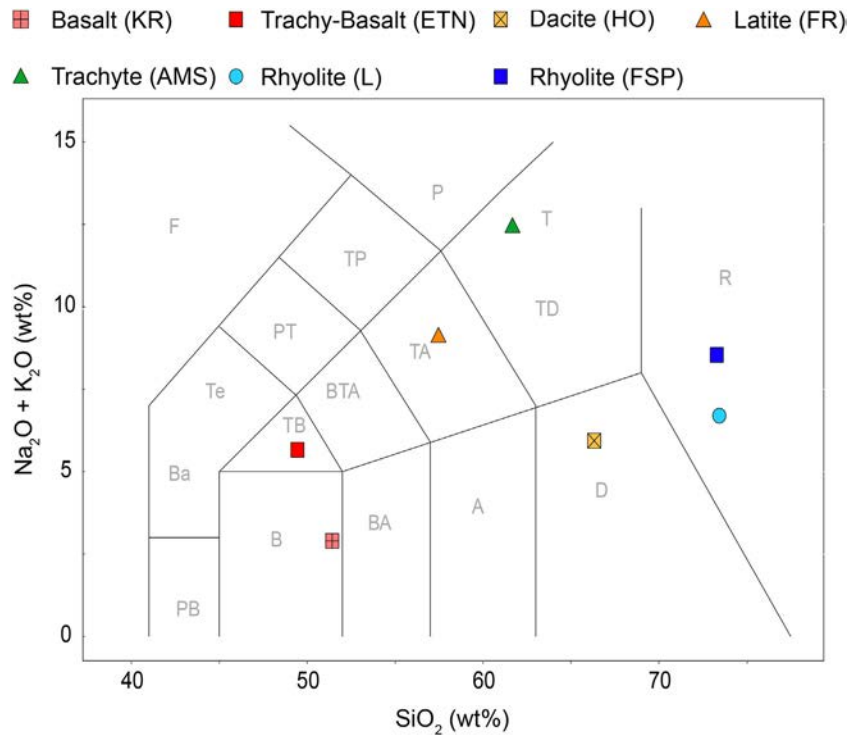
Table 2
Chemical composition (in wt%) of melt inclusions and glass embayments from Pantelleria Island (Italy). See Figs. 6, 7 and 9 for sample location.

Sample	SiO_2	TiO_2	Al_2O_3	$FeO_{tot.}$	MnO	MgO	CaO	Na_2O	K_2O	SO_2	P_2O_5	Cl
GT1	68.31	0.39	7.84	8.40	0.27	0.10	0.26	5.71	4.86	0.03	0.00	0.74
GT5	68.78	0.43	7.72	8.74	0.41	0.08	0.31	5.77	5.07	0.06	0.02	0.90
GT6	67.48	0.47	7.66	7.93	0.31	0.11	0.34	6.05	4.65	0.09	0.04	1.12
GT8	67.25	0.44	7.39	7.39	0.31	0.08	0.26	6.07	4.97	0.13	0.01	1.00
GT9	68.85	0.45	7.84	8.06	0.32	0.12	0.33	4.73	4.75	0.07	0.04	1.02
CDG1	66.34	0.57	9.50	8.59	0.32	0.23	1.30	6.90	4.25	0.05	0.07	1.02
CDG4	67.49	0.60	9.75	8.03	0.26	0.14	0.59	6.65	4.60	0.04	0.04	0.61

Fig. 1. TAS (total alkali versus silica) diagram showing the composition of all samples used in this study. KR and HO glasses were synthesised for this study, while all other glasses were previously synthesised (see Table 1 for samples reference). Abbreviations in the plot mean: PB – picrobasalt, B – basalt, BA – basaltic andesite, A – andesite, D – dacite, R – rhyolite, TB – trachybasalt, BTA – basaltic trachyandesite, TA – trachyandesite, TD – trachydacite, T – trachyte, Ba – basanite, Te – tephrite, PT – phonotephrite, TP – tephriphonolite, P – phonolite, F – foidite. B).

source, but independently of the sample composition. Spectra acquired with the red laser (633 nm) show the highest intensity of this peak, while spectra collected using the blue laser (455 nm) display the lowest intensity.

4. Measuring the degree of "nanotilization" of synthetic glasses

As demonstrated above, the $Fe^{3+}/Fe_{tot.}$ ratio in the glass directly correlates with the intensity of the band at ~970 cm^{-1} regardless of the excitation source, while the occurrence of magnetite nanolites results in a peak at 670–690 cm^{-1} whose intensity depends on the laser wavelength. Recently, Di Genova et al. (2017b) showed that the development of the nanolite peak is associated with a proportional decrease of the band at ~970 cm^{-1}. This implies that magnetite nanolite precipitation occurs via transfer of Fe_2O_3 from the melt to the crystal structure. Based on these observations, we introduce a new index (N#) to quantify this transfer and, thus, the degree of "*nanotilization*" of volcanic glasses (i.e. how much of the total Fe_2O_3 has precipitated into crystals from the melt). It should be noted that, according to recent TEM observations on volcanic glasses (Mujin et al., 2017), the melt depletion of the Fe_2O_3 resulting from the nucleation and growth of nanolites is mainly controlled by the crystallization of magnetite and/or pyroxene. In our synthetic samples, however, we observed the occurrence of only magnetite and thus, here, N# refers to the "*nanotilization*" controlled by the crystallization of magnetite.

For each spectrum, we calculate (Table 1) the nanolite number N# as follows:

$$N\# = \frac{I_{670-690}}{I_{970}} \tag{1}$$

where $I_{670-690}$ and I_{970} represent the spectral intensity of the nanolite peak (between 670 and 690 cm^{-1}) and the Fe^{3+} band (~970 cm^{-1}), respectively. This index increases with increasing degree of nanotilization

and is equal to zero for a nanolite-free glass. In Fig. 4a–f we report the Long- and baseline-corrected spectra of nanolite-bearing glasses collected with the three different lasers.

Fig. 5 shows the calculated N# as a function of the laser wavelength. Due to the variable intensity for the same sample of the nanolite peak with laser wavelength (Fig. 3a–f), N# changes depending on the excitation source as a result of the differing laser coupling and, thus, the signal to background ratios for the ~670–690 cm^{-1} and the 970 cm^{-1} band. Therefore, comparative studies need to be performed using the same laser wavelength. The basaltic sample (KR3) exhibits the highest degree of nanotilization (Table 1 and Fig. 5), followed by the latitic (FR3.8), dacitic (HO2) and rhyolitic (L) samples. On the other hand, the trachytic (AMS4) and trachy-basaltic (ETN3.8) are characterized by the lowest N# (Table 1 and Fig. 5).

5. Discussion: Nano-heterogeneity of natural products

Although to date little is known about the systematics of nanolite precipitation in magma, recent studies based on textural, geochemical, and experimental analyses of glasses and melts suggest that nanolites precipitate predominantly during magma ascent (Di Genova et al., 2017a; Mujin et al., 2017; Mujin and Nakamura, 2014). In order to explore the possibility of retrieving information on the changes of the melt structure during the eruption, we acquired Raman spectra of closed, partially degassed, and leaked melt inclusions (MIs). These different glasses can provide information on the structure of the melt frozen in when it crossed the glass transition temperature during the eruptive event.

Pantellerites are one of the most enigmatic peralkaline rhyolites since they are enriched in iron and characterized by an extraordinarily low viscosity, but nonetheless often feed high intensity (VEI) explosive eruptions (Civetta et al., 1984; Webster et al., 1993). In spite of the wealth of studies (Campagnola et al., 2016; Di Genova et al., 2013; Hughes et al., 2017; Lanzo et al., 2013), key issues on the fragmentation
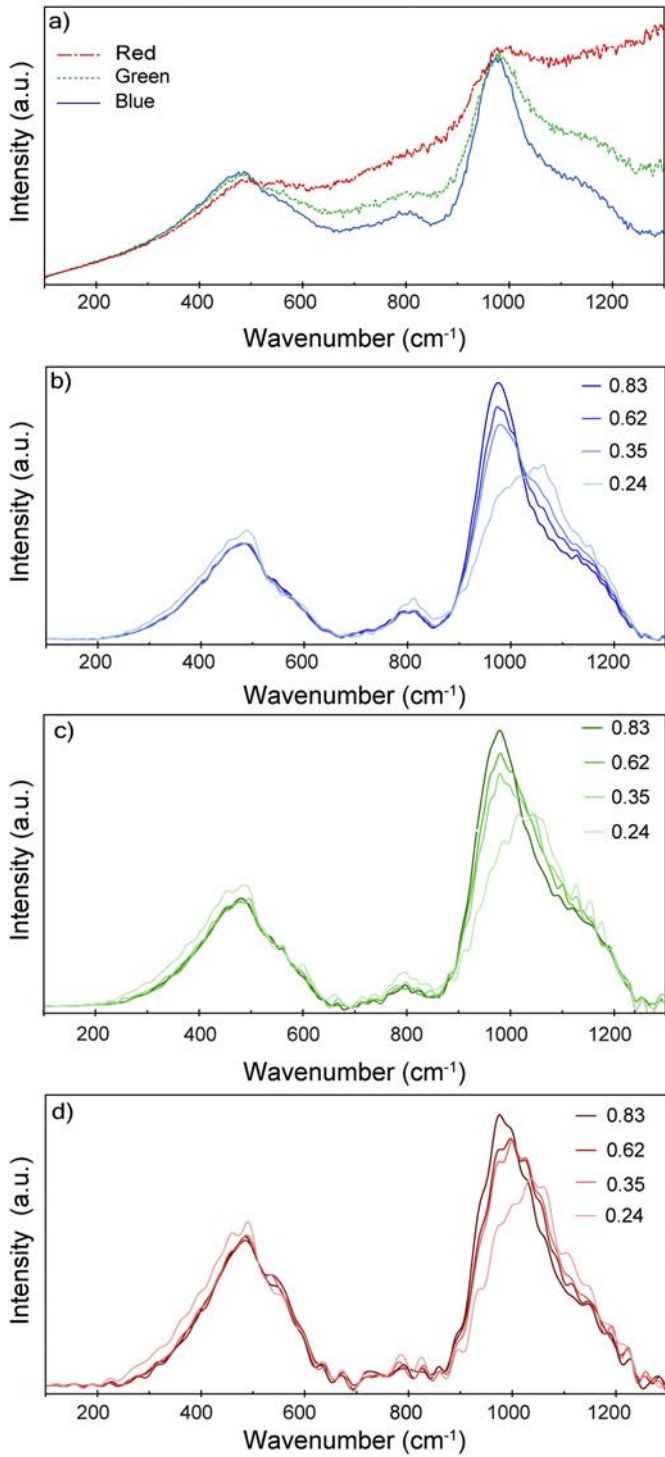
Fig. 2. (a) Long-corrected Raman spectra of the Fe^{3+}-rich rhyolitic glass (Fsp1 sample, $Fe^{3+}/Fe_{tot.} = 0.83$) collected with the three different lasers before background subtraction. The signal/background ratio increases from the red (633 nm), to green (532 nm) to blue (455 nm) laser. (b, c, d) Long- and background corrected and area normalised Raman spectra of iron-rich rhyolitic glasses (Fsp series, Table 1) characterized by varying Fe^{3+}/Fe_{tot} ratios (numbers in the legend). Spectra were acquired using three different lasers: b) blue, c) green, d) red. With increasing the iron oxidation state of the glass, the band at ~970 cm^{-1} increases independent of the excitation source. The 1040 cm^{-1} contribution is dominant in Fe_2O_3-poor pantelleritic glass (see the text for more details). (For interpretation of the references to colour in this figure legend, the reader is referred to the web version of this article.)

dynamics of these magmas remain elusive. We collected pantelleritic samples erupted during two explosive eruptions of different intensity at Pantelleria island (Italy):1) the basal vitrophyre of the caldera-
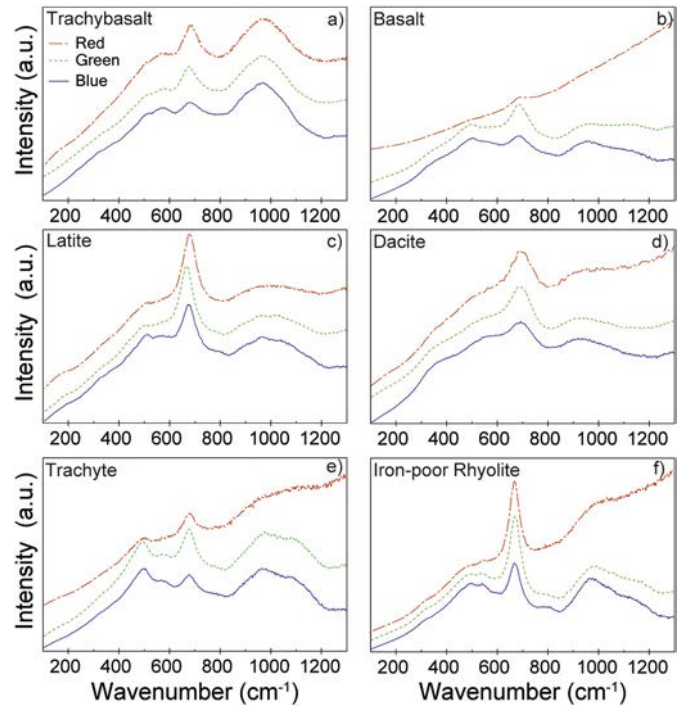
Fig. 3. Long-corrected spectra of nanolite-bearing glasses with different chemical composition acquired with the 455 nm (blue), 532 nm (green), and 633 nm (red) lasers before baseline subtraction. a) trachybasalt (ETN3.8), b) basalt (KR3), c) latite (FR3.8), d) dacite (HO2), e) trachyte (AMS4), f) calcalkaline rhyolite (L). The sample composition is reported in Table 1. (For interpretation of the references to colour in this figure legend, the reader is referred to the web version of this article.)
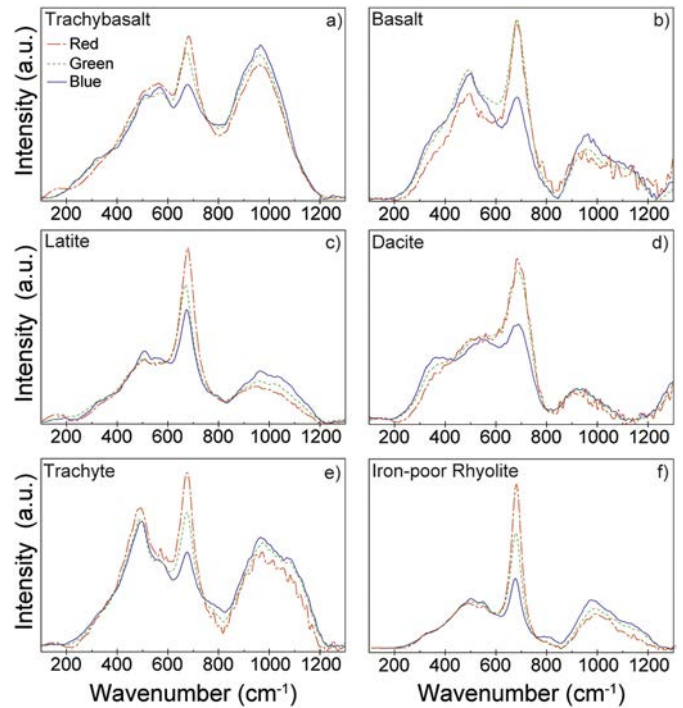

Fig. 4. Long- and baseline-corrected and area normalised Raman spectra of the nanolite-bearing samples acquired with the 455 nm (blue), 532 nm (green), and 633 nm (red) lasers. a) trachybasalt (ETN3.8), b) basalt (KR3), c) latite (FR3.8), d) dacite (HO2), e) trachyte (AMS4), f) calcalkaline rhyolite (L). Sample compositions are reported in Table 1. (For interpretation of the references to colour in this figure legend, the reader is referred to the web version of this article.)
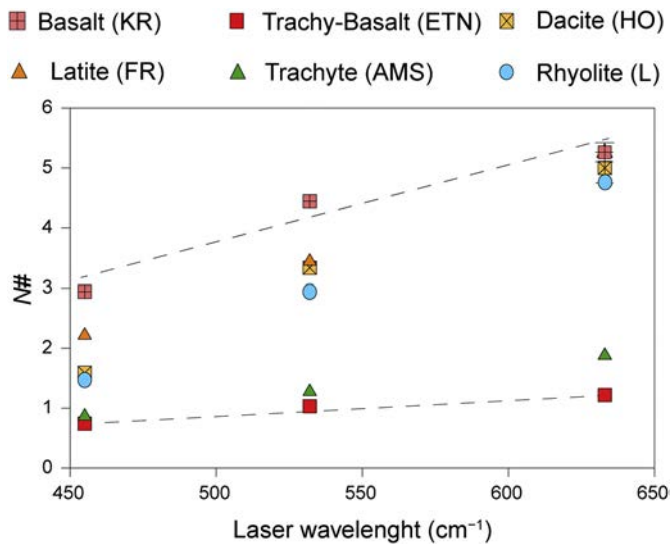
Fig. 5. Nanolite number (*N#*, Eq. 1) as a function of the laser wavelength. The dotted lines are intended as a guide for the eye.

forming eruption of the Green Tuff deposit (45–50 ka, Civetta et al., 1984) and 2) spatters erupted during the weak-Strombolian activity of Cuddia del Gallo cone (~6 ka, Gioncada and Landi, 2010).

Fig. 6a shows an hourglass MI hosted in diopside and an external melt trapped between the crystal surface and a bubble. Raman spectra and their locations are shown in Fig. 6b and a, respectively. The main contribution to the Raman spectra is located at ~970 cm^{-1}. The Fe^{3+}/ $Fe_{tot.}$ ratio of the Raman spectra is ~0.5 and was constrained in reference to spectra from samples of the same composition but different iron oxidation state (Di Genova et al., 2016a; Di Muro et al., 2009).

The H_2O content of the glass decreases from ~1.3 wt% for the GT1 and GT2 spectra (Fig. 6a–b) to essentially water free at the outside of the leaked melt inclusion (spectra GT4 and GT5). Furthermore, the first three spectra (GT1, GT2 and GT3) exhibit a contribution at ~670 cm^{-1} (Fig. 6b) indicating the presence of Fe-bearing nanocrystals. In the presented case the spectral signature of the host mineral (diopside) exhibits a similar contribution at ~670 cm^{-1} (Fig. 6b) that is to be evaluated in order to exclude eventual misidentification of the Raman feature. The host mineral also shows a prominent peak at ~1015 cm^{-1} and two weaker contributions at ~320 and ~390 cm^{-1}. Although the latter peaks were not observed in the glass spectra GT1, GT2 and GT3, we observed the development of a slight shoulder at ~1000 cm^{-1}, a lower position with respect to the main peak of the diopside. Additionally, while the full width at half maximum (FWHM) of the 670 cm^{-1} peak of the diopside (Fig. 6b), due to the presence of Fe_2O_3 in its crystalline structure, is narrow (~15–20 cm^{-1}, Lafuente et al., 2015), the FWHM of the 670 cm^{-1} peak of GT1, GT2 and GT3 spectra is significantly broader (~40–45 cm^{-1}) and similar to that observed in the Fe_2O_3 nanolite-bearing glasses in Fig. 4a–f and reported by previous studies (Figs. 3 in Di Muro et al., 2006a, 2006b). This suggests the incipient crystallization of diopside, resulting in the development of hybrid features between the quenched melt structure and the crystal structure.

Overall, the evolution of the spectral signature from GT1 to GT5 is paralleled by a decrease in the H_2O content of the melt which results in an increase in melt viscosity and, thus, a decrease in element diffusivity from inside the inclusion to the outside. Assuming a similar thermal path for the melt in the inclusion and the outside, this allows for a higher potential of nanolite formation in the lower viscosity, water-rich and higher diffusivity inside of the melt inclusion with respect to the outside, where the melt is efficiently quenched to a glass during the eruption. The relatively high-water content may promote oxidising conditions of the system (Humphreys et al., 2015) and, combined to fast quench rate (Di Genova et al., 2017b; Di Muro et al., 2006a), induced
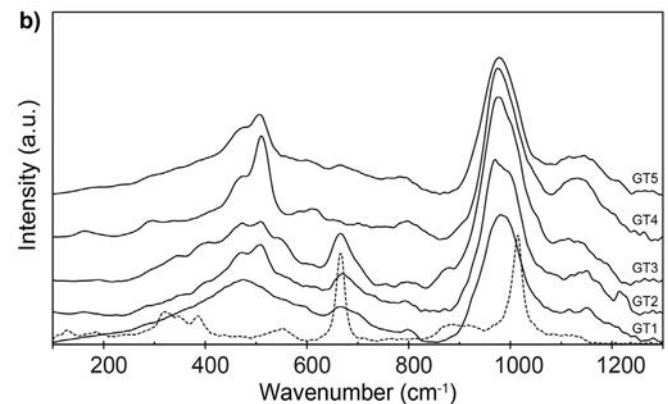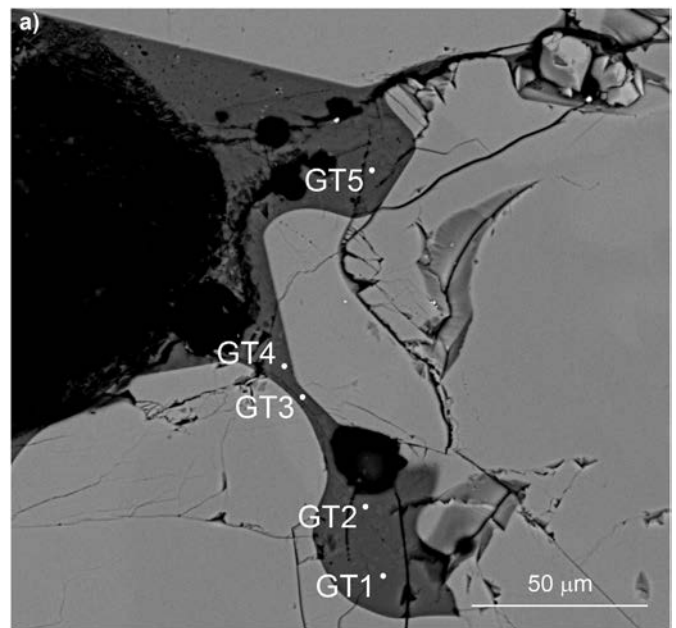

Fig. 6. a) SEM image from an hourglass melt inclusion from the Green Tuff vitrophyre in contact with the melt surrounding the host mineral (diopside). Labels indicate the location of Raman spectra reported in b). Hydrous and nanolite-bearing glass was detected in the glass embayment (GT1, GT2 and GT3 spectra), while dry glass characterized by incipient crystallization of feldspar was found on the outside of the inclusion (GT4 and GT5 spectra). The Raman spectrum of the host mineral is also reported (dashed). (For interpretation of the references to colour in this figure legend, the reader is referred to the web version of this article.)

the formation of magnetite nanolites during degassing. This process, however, is not restricted to magnetite only and can also occur during the crystallization of other phases such as for example pyroxene and plagioclase (Mujin et al., 2017). In fact, degassing-induced crystallization of both these phases is well documented for basaltic lavas (Applegarth et al., 2013; Lipman et al., 1985) but has not been described for pantelleritic melts. This is likely due to the small scale of the crystals forming during degassing, which required new techniques for their identification, such as presented here. The spectra collected at the outside of the melt inclusion (spectra GT4 and GT5, Fig. 6b) show two peaks at ~470 and ~510 cm^{-1} that are characteristics of Raman features in feldspar. However, these peaks are broader and shifted to a lower wavenumber (-7 cm^{-1}, Fig. 7b) compared to the spectrum of the adjacent feldspar (dashed line in Fig. 7b). This suggests incipient feldspar nucleation within the melt during ascent and/or quenching. Such pre-crystalline precipitates have been identified in experimental studies on supersaturated hydrothermal fluids crystallizing silicates at high temperature and pressure (Manning, 2018).

Fig. 7a shows a leaked feldspar-hosted MI containing two bubbles of ~10 μm diameter. The spectrum collected from the interior of the MI
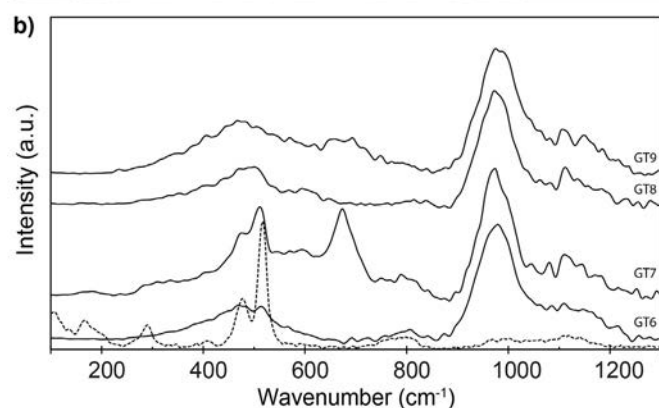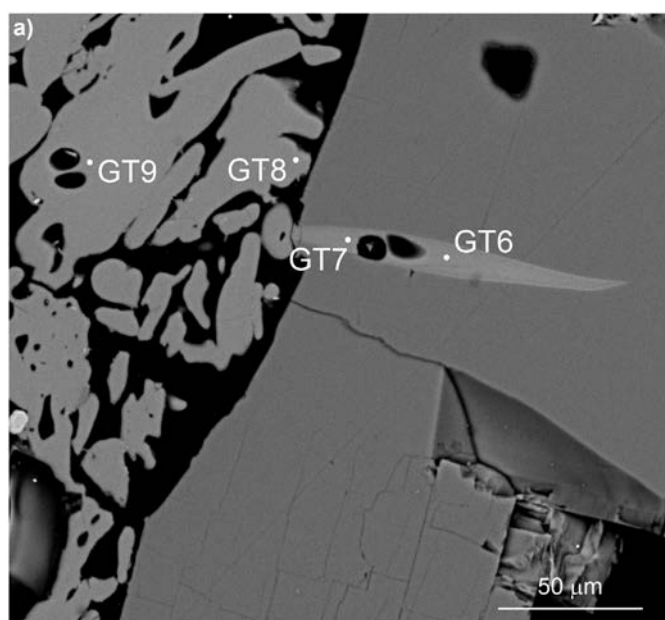
Fig. 7. a) SEM image of a feldspar hosted melt inclusion from the Green Tuff vitrophyre. Labels indicate the location of Raman spectra reported in b). Raman spectra revealed the presence of a nanolite-free glass in the interior of the melt inclusion (GT6 spectrum) and around the crystal (GT8 and GT9 spectra), whereas nanolite-bearing glass was detected in the vicinity of the bubble (GT7 spectrum). The Raman spectrum of the host mineral is reported for reference (dashed). (For interpretation of the references to colour in this figure legend, the reader is referred to the web version of this article.)
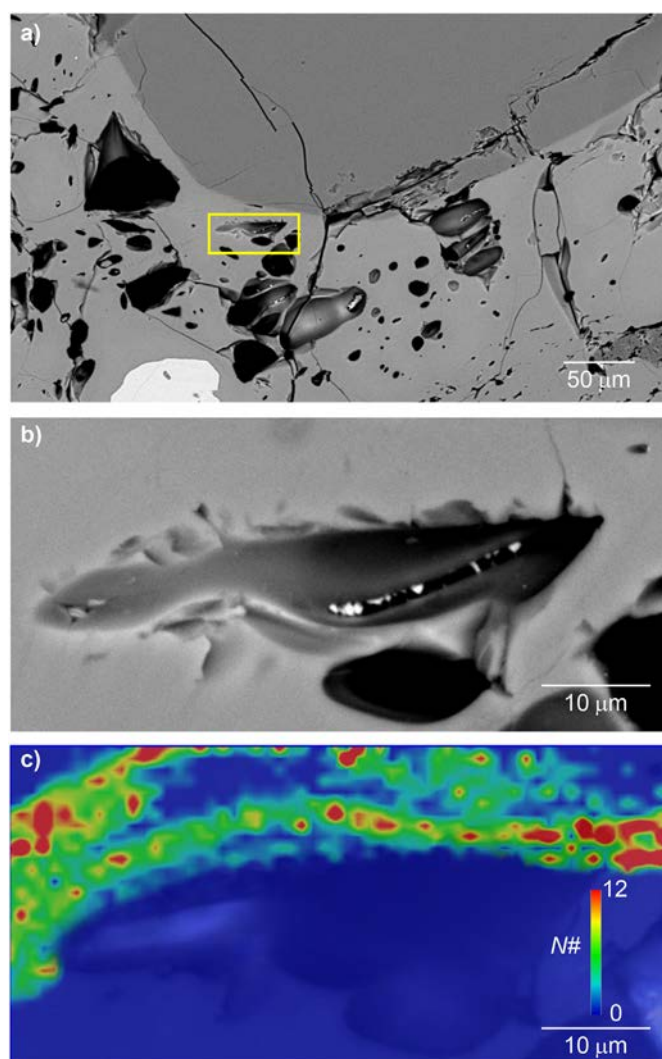

Fig. 8. a) SEM image of the Green Tuff vitrophyre groundmass. The square indicates the area (b) where Raman spectra were collected to map (c) the degree of *nanotilization* around the bubble. Hot colours indicate higher *nanotilization* degree, while cold colours indicate lower *nanotilization* degree according to N# (Eq. 1). Blue represents a nanolite-free glass. Some of the spectra on the bottom- whitish-side of the bubble show high fluorescence resulting in the inability to determine the N#. For those spectra we interpolate the N# of the neighbouring spectra. (For interpretation of the references to colour in this figure legend, the reader is referred to the web version of this article.)

(GT6, Fig. 7b) exhibits the typical features of pantelleritic glasses (Fig. 2a–d), while the spectrum collected close to the bubble surface (GT7, Fig. 7b) is characterized by the ~670 cm^{-1} nanolite peak which is not present in the spectrum of the host mineral (Fig. 7b). Moreover, as reported before, the difference in Raman shift of the two peaks located at ~470, ~510 cm^{-1} with respect to the host mineral spectrum, together with the absence of crystalline peaks at ~170 and 290 cm^{-1} in the MIs spectra, suggest that the melt structure has undergone incipient feldspar crystallization below available resolution. We also inspected the groundmass glass of the basal vitrophyre in order to study its structure. In Fig. 8a–b we report a BSE-SEM image of 1800 μm^2 over which we acquired 1800 Raman spectra. We found that, albeit the BSE-SEM image suggests this area to be composed of homogenous glass, the Raman spectra collected from the matrix groundmass were highly heterogenous at the nanoscale. In order to quantify and visualize the degree of nanotilization, we calculated the N# (Eq. 1) for each spectrum. Fig. 8c shows a heat map visualizing the degree of nanolitization using a colour gradient from cold (blue, nanolite-free glass, low N#) to hot (red, nanolite-bearing glass, high N#). The distribution of colours shows the coexistence of two domains 1) a pure, nanolite free glass and 2) an extremely nano-heterogenous glass.

In line with in situ observations of bubble nucleation in silicate melts (Masotta et al., 2014; Pleše et al., 2018 and reference therein), textural observations of volcanic products (Applegarth et al., 2013; Lipman et al., 1985) and experimental results (see Shea, 2017 for a review), the development of incipient crystalline features in the Raman spectra on the inside of vesiculating melt inclusions (Figs. 6 and 7) suggest that the nanotilization stimulated/facilitated the exsolution of volatile components of the magma by providing nucleation sites that promote bubble formation, increased the melt viscosity (Di Genova et al., 2017a) and, thereby, contribute to enhancing the explosivity of volcanic eruptions.

We now expand this analysis to the lower intensity Strombolian type eruptions from the Cuddia del Gallo eruption by including flattened pantelleritic spatters. This allows us to evaluate whether secondary processes (e.g. annealing and potential oxidation) may have induced the observed structural heterogeneities of the glass.

In Fig. 9a we show a SEM image of MIs from spatters erupted during this event. The location of the acquired Raman spectra is reported in Fig. 9a, while the spectra are reported in Fig. 9b. We analysed three
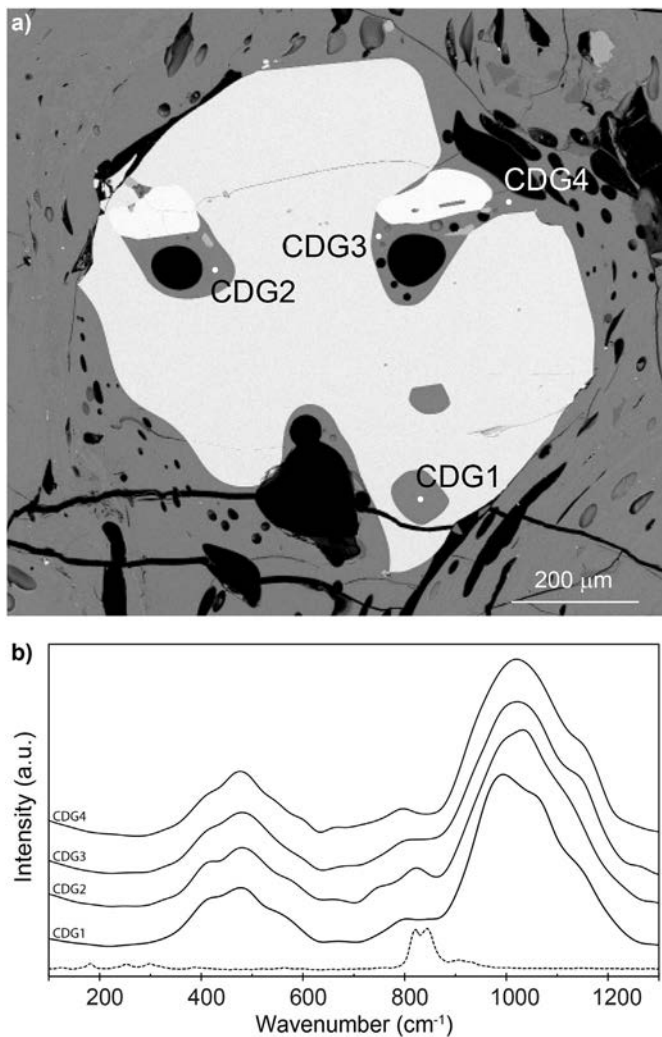
Fig. 9. a) SEM image of olivine hosted melt inclusions and glass embayment from the Cuddia del Gallo spatter (Pantelleria Island, Italy). Labels indicate the location of Raman spectra reported in b). The Raman spectrum of the host mineral is also reported (dashed). Although the sample shows a certain degree of textural heterogeneity of the groundmass, Raman spectra acquired along the sample confirmed that the glass matrix is systematically more reduced than the Green Tuff vitrophyre groundmass. (For interpretation of the references to colour in this figure legend, the reader is referred to the web version of this article.)

characteristic melt inclusions; 1) a closed MI (CDG1), 2) a partially open MI coexisting with a bubble (CDG2), and 3) a glass embayment containing bubbles (CDG3–4).

The Raman spectra in the region at ~3550 cm^{-1} (Fig. A.1.) revealed that only the closed and bubble-free MI (CDG1) contains water, while the embayments (CDG2–4) are anhydrous. Overall, comparison of the results obtained from Cuddia del Gallo spatter with those from the Green Tuff vitrophyre, suggests that all the MIs from the spatters of Cuddia del Gallo (CDG1–4, Fig. 9b) are more reduced (Di Genova et al., 2016a; Di Muro et al., 2009) with respect to the MIs of the Plinian eruption. This is inferred from the extremely weak contribution at ~970 cm^{-1} of the spatter spectra (Fig. 9b) with respect to those of the Green Tuff vitrophyre (Fig. 7a, see Di Genova et al., 2016a; Di Muro et al., 2009 for further detail on how to estimate the Fe^{3+}/Fe$_{tot.}$ ratio of glasses). Furthermore, the nanotilization of the melt was more intense during the Plinian eruption (Green Tuff, Fig. 7b and 8c) than during the low-energetic Strombolian event at Cuddia del Gallo (Fig. 9b).

Previous studies estimated the pre-eruptive magmatic water content of pantelleritic eruptions at ~4–5 wt% (Di Carlo et al., 2010;

Gioncada and Landi, 2010; Kovalenko et al., 1988; Lanzo et al., 2013; Lowenstern and Mahood, 1991; Métrich et al., 2006; Neave et al., 2012; White et al., 2009). These data were collected on samples from a series of different eruptions on Pantelleria Island, including those studied here. Despite there being slight differences in pre-eruptive water content and oxygen fugacity among effusive and explosive eruptions, viscosity measurements of the effect of H$_2$O (Di Genova et al., 2013) and Fe^{3+}/Fe$_{tot.}$ ratio (Stabile et al., 2016; Stabile et al., 2017) on the melt viscosity demonstrated that pantelleritic melts are of extremely low viscosity, with respect to their calcalkaline counterparts, regardless of the water content and iron oxidation state. As a consequence of these low viscosities (and hence fast relaxation timescales), the calculated strain rates required for exceeding Maxwell's criterion and inducing brittle fragmentation in these melts are unrealistically high (Dingwell, 1996; Hughes et al., 2017; Papale, 1999). Furthermore, the crystal content measured in the eruptive products is relatively low; <20 vol% (Campagnola et al., 2016; Gioncada and Landi, 2010; Hughes et al., 2017; Lanzo et al., 2013; Neave et al., 2012; Rotolo et al., 2013). Therefore, the effect of solid particles on the magma viscosity is expected to be very low (Campagnola et al., 2016; Mader et al., 2013 and references therein) and not enough to explain the transition from effusive to explosive eruptions at Pantelleria Island (Civetta et al., 1984; Gioncada and Landi, 2010; Mahood and Hildreth, 1986; Rotolo et al., 2013). It thus appears that the pre-eruptive conditions, including chemical composition and eruptive temperature (Di Carlo et al., 2010; Gioncada and Landi, 2010; Lanzo et al., 2013; Neave et al., 2012; Rotolo et al., 2013; White et al., 2009), are not the decisive factor controlling the intensity of the eruptions occurred at Pantelleria Island. We propose that the increase in viscosity due to nanolite formation induces a rheologic transition pushing the melt across the viscous/brittle transition. This is supported by the presented nano-heterogeneities in melt inclusions of the Green Tuff eruption.

We suggest that future studies should focus on the identification and characterization of nanolites in natural products such as the method presented here or TEM in combination with FE-SEM analysis as presented by Mujin et al. (2017), and on the development of a systematic understanding of the dynamics of their formation in silicate melts at physical and chemical conditions relevant for volcanic eruptions. This will help better constrain the control of melt structure on the eruptive behaviour of volcanoes and on changes in their eruptive style.

6. Conclusions

The presented Raman spectra of synthetic glasses collected with different lasers demonstrate that the spectral fluorescence greatly decreases with decreasing laser wavelength, and blue lasers provide the best signal to background ratio, especially in iron-poor systems.

We further demonstrate that independent of the excitation source, the Raman features at ~670–690 and ~970 cm^{-1} are exclusively controlled by the presence of magnetite nanolites and changes in the Fe^{3+}/Fe$_{tot.}$ ratio of the glass, respectively. Based on this relationship we develop a new method for the use of Raman spectroscopy as a tool for identification of nanoscale heterogeneities in glasses and introduce the N# as a measure for the degree of nano-heterogeneity of silicate glasses. This approach is significantly faster and more cost-effective than previously used tools such as for example Transmission Electron Microscopy (TEM).

The spectroscopic and analytical results, obtained from melt inclusions and glass embayments of volcanic products erupted during Strombolian (Cuddia del Gallo) and Plinian (Green Tuff) eruptions at Pantelleria Island (Italy), help to unravel the importance of the incipient melt nanotilization for processes acting during explosive eruptions. The acquired Raman spectra show systematic variations along melt inclusions communicating with the surrounding. They document that nanolite occurrence is intimately related to degassing. Since both the precipitation of nanolites and loss of water from the melt result in

increasing magma viscosity, we suggest that nanolite growth in pantelleritic melts contributes to controlling the transition in the eruptive style of such a low viscosity magma.

Based on the data presented above, we propose that glass embayments can be used to study the dynamic evolution of the melt nanostructure during degassing and incipient crystallization prior to and during the eruption. Our contribution illustrates that Raman spectroscopy represents a fundamental tool to investigate the distribution of nanolites, estimate the water content as well as iron oxidation state of volcanic products, and link the nanostructure of silicate melts to the eruptive dynamics.

Acknowledgements

Appendix A. Supplementary data

Supplementary data to this article can be found online at https://doi.org/10.1016/j.lithos.2018.08.011.

References

Applegarth, L.J., Tuffen, H., James, M.R., Pinkerton, H., 2013. Degassing-driven crystallisation in basalts. Earth Sci. Rev. 116:1–16. https://doi.org/10.1016/j.earscirev.2012.10.007.

Ardia, P., Di Muro, A., Giordano, D., Massare, D., Sanchez-Valle, C., Schmidt, M.W., 2014. Densification mechanisms of haplogranite glasses as a function of water content and pressure based on density and Raman data. Geochim. Cosmochim. Acta 138:158–180. https://doi.org/10.1016/j.gca.2014.03.022.

Barone, G., Mazzoleni, P., Corsaro, R.A., Costagliola, P., Di Benedetto, F., Ciliberto, E., Gimeno, D., Bongiorno, C., Spinella, C., 2016. Nanoscale surface modification of Mt. Etna volcanic ashes. Geochim. Cosmochim. Acta 174:70–84. https://doi.org/10.1016/j.gca.2015.11.011.

Behrens, H., Roux, J., Neuville, D.R., Siemann, M., 2006. Quantification of dissolved H2O in silicate glasses using confocal microRaman spectroscopy. Chem. Geol. 229:96–112. https://doi.org/10.1016/j.chemgeo.2006.01.014.

Botcharnikov, R.E., Koepke, J., Holtz, F., McCammon, C., Wilke, M., 2005. The effect of water activity on the oxidation and structural state of Fe in a ferro-basaltic melt. Geochim. Cosmochim. Acta 69:5071–5085. https://doi.org/10.1016/j.gca.2005.04.023.

Bouhifd, M.A., Richet, P., Besson, P., Roskosz, M., Ingrin, J., 2004. Redox state, microstructure and viscosity of a partially crystallized basalt melt. Earth Planet. Sci. Lett. 218, 31–44. https://doi.org/10.1016/S0012-821x(03)00641-1.

Campagnola, S., Romano, C., Vona, A., Mastin, L.G., 2016. Confort 15 model of conduit dynamics: applications to Pantelleria Green Tuff and Etna 122 BC eruptions. Contrib. Mineral. Petrol. 171:1–25. https://doi.org/10.1007/s00410-016-1265-5.

Civetta, L., Cornette, Y., Crisci, G., Gillot, P.Y., Orsi, G., Requejo, C.S., 1984. Geology, geochronology and chemical evolution of the island of Pantelleria. Geol. Mag. 121:541. https://doi.org/10.1017/S0016756800030703.

Di Carlo, I., Rotolo, S.G., Scaillet, B., Buccheri, V., Pichavant, M., 2010. Phase equilibrium constraints on pre-eruptive conditions of recent felsic explosive volcanism at Pantelleria Island, Italy. J. Petrol. 51:2245–2276. https://doi.org/10.1093/petrology/egq055.

Di Genova, D., Romano, C., Hess, K.-U., Vona, A., Poe, B.T., Giordano, D., Dingwell, D.B., Behrens, H., 2013. The rheology of peralkaline rhyolites from Pantelleria Island. J. Volcanol. Geotherm. Res. 249, 201–216.

Di Genova, D., Romano, C., Alletti, M., Misiti, V., Scarlato, P., 2014a. The effect of CO2 and H2O on Etna and Fondo Riccio (Phlegrean Fields) liquid viscosity, glass transition temperature and heat capacity. Chem. Geol. 377:72–86. https://doi.org/10.1016/j.chemgeo.2014.04.001.

Di Genova, D., Romano, C., Giordano, D., Alletti, M., 2014b. Heat capacity, configurational heat capacity and fragility of hydrous magmas. Geochim. Cosmochim. Acta 142:314–333. https://doi.org/10.1016/j.gca.2014.07.012.

Di Genova, D., Morgavi, D., Hess, K.-U., Neuville, D.R., Borovkov, N., Dingwell, D.B., 2015. Approximate chemical analysis of volcanic glasses using Raman spectroscopy. J. Raman Spectrosc. 46:1235–1244. https://doi.org/10.1002/jrs.4751.

Di Genova, D., Hess, K.-U., Chevrel, M.O., Dingwell, D.B., 2016a. Models for the estimation of Fe3+/Fetot. Ratio in terrestrial and extra- terrestrial alkali- and iron-rich silicate glasses using Raman spectroscopy. Am. Mineral. 101, 943–952.

Di Genova, D., Kolzenburg, S., Vona, A., Chevrel, M.O., Hess, K.-U., Neuville, D.R., Ertel-Ingrisch, W., Romano, C., Dingwell, D.B., 2016b. Raman spectra of Martian glass analogues: a tool to approximate their chemical composition. J. Geophys. Res. Planets 121:740–752. https://doi.org/10.1002/2016JE005010.

Di Genova, D., Kolzenburg, S., Wiesmaier, S., Dallanave, E., Neuville, D.R., Hess, K.-U., Dingwell, D.B., 2017a. A chemical tipping point governing mobilization and eruption style of rhyolitic magma. Nature 552:235–238. https://doi.org/10.1038/nature24488.

Di Genova, D., Sicola, S., Romano, C., Vona, A., Fanara, S., Spina, L., 2017b. Effect of iron and nanolites on Raman spectra of volcanic glasses: reassessment of existing strategies to estimate the water content. Chem. Geol. 475:76–86. https://doi.org/10.1016/j.chemgeo.2017.10.035.

Di Genova, D., Vasseur, J., Hess, K.-U., Neuville, D.R., Dingwell, D.B., 2017c. Effect of oxygen fugacity on the glass transition, viscosity and structure of silica- and iron-rich magmatic melts. J. Non-Cryst. Solids 470:78–85. https://doi.org/10.1016/j.jnoncrysol.2017.05.013.

Di Muro, A., Giordano, D., Villemant, B., Montagnac, G., Scaillet, B., Romano, C., 2006a. Influence of composition and thermal history of volcanic glasses on water content as determined by micro-Raman spectrometry q. Appl. Geochem. 21:802–812. https://doi.org/10.1016/j.apgeochem.2006.02.009.

Di Muro, A., Villemant, B., Montagnac, G., Scaillet, B., Reynard, B., 2006b. Quantification of water content and speciation in natural silicic glasses (phonolite, dacite, rhyolite) by confocal microRaman spectrometry. Geochim. Cosmochim. Acta 70:2868–2884. https://doi.org/10.1016/j.gca.2006.02.016.

Di Muro, A., Métrich, N., Mercier, M., Giordano, D., Massare, D., Montagnac, G., 2009. Micro-Raman determination of iron redox state in dry natural glasses: application to peralkaline rhyolites and basalts. Chem. Geol. 259:78–88. https://doi.org/10.1016/j.chemgeo.2008.08.013.

Dingwell, D.B., 1996. Volcanic dilemma: flow or blow? Science 273, 1054–1055.

Dingwell, D.B., Virgo, D., 1987. The effect of oxidation state on the viscosity of melts in the system Na2O-FeO-Fe2O3-SiO2. Geochim. Cosmochim. Acta 51, 195–205.

Dingwell, D.B., Brearley, M., Dickinson Jr., E., 1988. Melt densities in the Na2O-FeO-Fe2O3-SiO2 system and the partial molar volume of tetrahedrally-coordinated ferric iron in silicate melts. Geochim. Cosmochim. Acta 52, 2467–2475.

Fox, K.E., Furukawa, T., White, W.B., 1982. Transition metal ions in silicate melts. Part 2. Iron in sodium silicate glasses. Phys. Chem. Glasses 23 (5), 169–178.

Gardner, J.E., Denis, M.-H.H., 2004. Heterogeneous bubble nucleation on Fe-Ti oxide crystals in high-silica rhyolitic melts. Geochim. Cosmochim. Acta 68:3587–3597. https://doi.org/10.1016/j.gca.2004.02.021.

Gioncada, A., Landi, P., 2010. The pre-eruptive volatile contents of recent basaltic and pantelleritic magmas at Pantelleria (Italy). J. Volcanol. Geotherm. Res. 189:191–201. https://doi.org/10.1016/j.jvolgeores.2009.11.006.

Giordano, D., Russell, J.K., Dingwell, D.B., 2008. Viscosity of magmatic liquids: a model. Earth Planet. Sci. Lett. 271:123–134. https://doi.org/10.1016/j.epsl.2008.03.038.

Giordano, D., Nichols, A.R.L., Potuzak, M., Di Genova, D., Romano, C., Russell, J.K., 2015. Heat capacity of hydrous trachybasalt from Mt Etna: comparison with CaAl2Si2O8 (An)–CaMgSi2O6 (Di) as basaltic proxy compositions. Contrib. Mineral. Petrol. 170:48. https://doi.org/10.1007/s00410-015-1196-6.

Gonnermann, H.M., Manga, M., 2007. The fluid mechanics inside a volcano. Annu. Rev. Fluid Mech. 39:321–356. https://doi.org/10.1146/annurev.fluid.39.050905.110207.

Hammer, J.E., Cashman, K.V., Hoblitt, R.P., Newman, S., 1999. Degassing and microlite crystallization during pre-climactic events of the 1991 eruption of Mt. Pinatubo, Philippines. Bull. Volcanol. 60:355–380. https://doi.org/10.1007/s004450050238.

Hughes, E.C., Neave, D.A., Dobson, K.J., Withers, P.J., Edmonds, M., 2017. How to fragment peralkaline rhyolites: observations on pumice using combined multi-scale 2D and 3D imaging. J. Volcanol. Geotherm. Res. 336:179–191. https://doi.org/10.1016/j.jvolgeores.2017.02.020.

Hui, H.J., Zhang, Y., 2007. Toward a general viscosity equation for natural anhydrous and hydrous silicate melts. Geochim. Cosmochim. Acta 71:403–416. https://doi.org/10.1016/j.gca.2006.09.003.

Humphreys, M.C.S., Brooker, R.A., Fraser, D.G., Burgisser, A., Mangan, M.T., McCammon, C., 2015. Coupled interactions between volatile activity and Fe oxidation state during arc crustal processes. J. Petrol. 56:795–814. https://doi.org/10.1093/petrology/egv017.

Kolzenburg, S., Di Genova, D., Giordano, D., Hess, K.-U., Dingwell, D.B., 2018. The effect of oxygen fugacity on the rheological evolution of crystallizing basaltic melts. Earth Planet. Sci. Lett. 487:21–32. https://doi.org/10.1016/j.epsl.2018.01.023.

Kovalenko, V.I., Hervig, R.L., Sheridan, M.F., 1988. Ion microprobe analyses of trace elements in anorthoclase, hedenbergite, aenigmatite, quartz, apatite and glass in pantellerite: evidence for high water contents in pantellerite melt. Am. Mineral. 73, 1038–1045.

Kubicki, J.D., Toplis, M.J., 2002. Molecular orbital calcula- tions on aluminosilicate tricluster molecules: implications for the structure of aluminosilicate glasses. Am. Mineral. 87, 668–678.

Lafuente, B., Downs, R.T., Yang, H., Stone, N., 2015. The power of databases: the RRUFF project. Highlights Mineral. Crystallogr. https://doi.org/10.1515/9783110417104-003.

Lanzo, G., Landi, P., Rotolo, S.G., 2013. Volatiles in pantellerite magmas: a case study of the Green Tuff Plinian eruption (Island of Pantelleria, Italy). J. Volcanol. Geotherm. Res. 262:153–163. https://doi.org/10.1016/j.jvolgeores.2013.06.011.

Liebske, C., Behrens, H., Holtz, F., Lange, R.A., 2003. The influence of pressure and composition on the viscosity of andesitic melts. Geochim. Cosmochim. Acta 67, 473–485. https://doi.org/10.1016/S0016-7037(02)01139-0.

Lipman, P.W., Banks, N.G., Rhodes, J.M., 1985. Degassing-induced crystallization of basaltic magma and effect on lava rheology. Nature 317, 604–607.

Long, D.A., 1977. Raman Spectroscopy, in: Mcgraw-Hill. Mcgraw-Hill, p. 276.

Lowenstern, J.B., Mahood, G.A., 1991. New data on magmatic H2O contents of pantellerites, with implications for petrogenesis and eruptive dynamics at Pantelleria. Bull. Volcanol. 54, 78–83.

Mader, H.M., Llewellin, E.W., Mueller, S.P., 2013. The rheology of two-phase magmas: a review and analysis. J. Volcanol. Geotherm. Res. 257:135–158. https://doi.org/10.1016/j.jvolgeores.2013.02.014.

Mahood, G.A., Hildreth, W., 1986. Geology of the peralkaline volcano at Pantelleria, Strait of Sicily. Bull. Volcanol. 48, 143–172.

Manning, C.E., 2018. Fluids of the lower crust: deep is different. Annu. Rev. Earth Planet. Sci. 46, 67–97. https://doi.org/10.1146/annurev-earth-060614- 105224.

Masotta, M., Ni, H., Keppler, H., 2014. In situ observations of bubble growth in basaltic, andesitic and rhyodacitic melts. Contrib. Mineral. Petrol. 167:1–14. https://doi.org/10.1007/s00410-014-0976-8.

McMillan, P.F., 1984. Structural studies of silicate glasses and melts-applications and limitations of Raman spectroscopy. Am. Mineral. 69:622–644. https://doi.org/0003-004x/84/070E-0622$0.

McMillan, P.F., Piriou, B., 1982. The structures and vibrational spectra of crystals and glasses in the silica-alumina system. J. Non-Cryst. Solids 53, 279–298. https://doi.org/10.1016/0022-3093(82)90086-2.

Mercier, M., Di Muro, A., Giordano, D., Métrich, N., Lesne, P., Pichavant, M., Scaillet, B., Clocchiatti, R., Montagnac, G., 2009. Influence of glass polymerisation and oxidation on micro-Raman water analysis in alumino-silicate glasses. Geochim. Cosmochim. Acta 73:197–217. https://doi.org/10.1016/j.gca.2008.09.030.

Mercier, M., Di Muro, A., Métrich, N., Giordano, D., Belhadj, O., Mandeville, C.W., 2010. Spectroscopic analysis (FTIR, Raman) of water in mafic and intermediate glasses and glass inclusions. Geochim. Cosmochim. Acta 74:5641–5656. https://doi.org/10.1016/j.gca.2010.06.020.

Métrich, N., Susini, J., Foy, E., Farges, F., Massare, D., Sylla, L., Lequien, S., Bonnin-Mosbah, M., 2006. Redox state of iron in peralkaline rhyolitic glass/melt: X-ray absorption micro-spectroscopy experiments at high temperature. Chem. Geol. 231:350–363. https://doi.org/10.1016/j.chemgeo.2006.02.001.

Morizet, Y., Brooker, R.a., Iacono-Marziano, G., Kjarsgaard, B.a., 2013. Quantification of dissolved CO2 in silicate glasses using micro-Raman spectroscopy. Am. Mineral. 98: 1788–1802. https://doi.org/10.2138/am.2013.4516.

Mujin, M., Nakamura, M., 2014. A nanolite record of eruption style transition. Geology 42: 611–614. https://doi.org/10.1130/G35553.1.

Mujin, M., Nakamura, M., Miyake, A., 2017. Eruption style and crystal size distributions: crystallization of groundmass nanolites in the 2011 Shinmoedake eruption. Am. Mineral. 102:2367–2380. https://doi.org/10.1186/s12986.

Mysen, B.O., 1999. Structure and properties of magmatic liquids: from haplobasalt to haploandesite. Geochim. Cosmochim. Acta 63, 95–112.

Mysen, B.O., Richet, P., 2005. Silicate Glasses and Melts-Properties and Structure (Amsterdam).

Mysen, B.O., Virgo, D., Seifert, F.a., 1982. The structure of silicate melts: implications for chemical and physical properties of natural magma. Rev. Geophys. Space Phys. https://doi.org/10.1029/RG020i003p00353.

Mysen, B.O., Virgo, D., Scarfe, C.M., Cronin, D.J., 1985. Viscosity and structure of iron- and aluminum-bearing calcium silicate melts at 1 atm of not. Am. Mineral. 70, 487–498.

Neave, D.A., Fabbro, G., Herd, R.A., Petrone, C.M., Edmonds, M., 2012. Melting, differentiation and degassing at the Pantelleria volcano, Italy. J. Petrol. 53:637–663. https://doi.org/10.1093/petrology/egr074.

Newhall, C., Self, S., Robock, A., 2018. Anticipating future Volcanic Explosivity Index (VEI) 7 eruptions and their chilling impacts. Geosphere 14:572–603. https://doi.org/10.1130/GES01513.1.

Papale, P., 1999. Strain-induced magma fragmentation in explosive eruptions. Nature 397, 425–428.

Petford, N., 2003. Rheology of granitic magmas during ascent and emplacement. Rev. Lit. Arts Am.:399–427. https://doi.org/10.1146/annurev.earth.31.100901.141352.

Pistolesi, M., Rosi, M., Cion, R., Cashman, K.V., Rossotti, A., Aguilera, E., 2011. Physical volcanology of the post-twelfth-century activity at Cotopaxi volcano, Ecuador: behavior of an andesitic central volcano. Bull. Geol. Soc. Am. 123:1193–1215. https://doi.org/10.1130/B30301.1.

Pleše, P., Higgins, M.D., Mancini, L., Lanzafame, G., Brun, F., Fife, J.L., Casselman, J., Baker, D.R., 2018. Dynamic observations of vesiculation reveal the role of silicate crystals in bubble nucleation and growth in andesitic magmas. Lithos 296–299:532–546. https://doi.org/10.1016/j.lithos.2017.11.024.

Poe, B.T.T., Romano, C., Di Genova, D., Behrens, H., Scarlato, P., 2012. Mixed electrical conduction in a hydrous pantellerite glass. Chem. Geol. 320–321:140–146. https://doi.org/10.1016/j.chemgeo.2012.05.023.

Rotolo, S.G., Scaillet, S., La Felice, S., Vita-Scaillet, G., 2013. A revision of the structure and stratigraphy of pre-Green Tuff ignimbrites at Pantelleria (Strait of Sicily). J. Volcanol. Geotherm. Res. 250:61–74. https://doi.org/10.1016/j.jvolgeores.2012.10.009.

Schiavi, F., Bolfan-Casanova, N., Withers, A.C., Médard, E., Laumonier, M., Laporte, D., Flaherty, T., Gómez-Ulla, A., 2018. Water quantification in silicate glasses by Raman spectroscopy: correcting for the effects of confocality, density and ferric iron. Chem. Geol. 483:312–331. https://doi.org/10.1016/j.chemgeo.2018.02.036.

Sharma, S.K., Mammone, J.F., Nicol, M.F., 1981. Raman investigation of ring configurations in vitreous silica. Nature https://doi.org/10.1038/292140a0.

Sharma, S.K., Cooney, T.F., Wang, Z.F., Van der Laan, S., 1997. Raman band assignments of silicate and germanate glasses using high-pressure and high-temperature spectral data. J. Raman Spectrosc. 28, 697–709.

Shea, T., 2017. Bubble nucleation in magmas: a dominantly heterogeneous process? J. Volcanol. Geotherm. Res. 343:155–170. https://doi.org/10.1016/j.jvolgeores.2017.06.025.

Stabile, P., Webb, S.L., Knipping, J.L., Behrens, H., Paris, E., Giuli, G., 2016. Viscosity of pantelleritic and alkali silicate melts: effect of Fe redox state and Na/(Na+K) ratio. Chem. Geol. 442:73–82. https://doi.org/10.1016/j.chemgeo.2016.09.003.

Stabile, P., Giuli, G., Cicconi, M.R., Paris, E., Trapananti, A., Behrens, H., 2017. The effect of oxygen fugacity and Na/(Na+K) ratio on iron speciation in pantelleritic glasses. J. Non-Cryst. Solids 0–1. https://doi.org/10.1016/j.jnoncrysol.2017.09.051.

Thomas, R., 2000. Determination of water contents of granite melt inclusions by confocal laser Raman microprobe spectroscopy. Am. Mineral. 85, 868–872.

Toplis, M.J., Carroll, M.R., 1995. An experimental study of the influence of oxygen fugacity on Fe-Ti oxide stability, phase relations, and mineral- melt equilibria in ferro-basaltic systems. J. Petrol. 36, 1137–1170.

Toplis, M.J., Dingwell, D.B., Lenci, T., 1997. Peraluminous viscosity maxima in Na2O-Al2O3-SiO2 liquids : the role of triclusters in tectosilicate melts. Geochim. Cosmochim. Acta 61, 2605–2612.

van Keken, P.E., 2003. The structure and dynamics of the mantle wedge. Earth Planet. Sci. Lett. 215, 323–338. https://doi.org/10.1016/S0012-821X(03)00460-6.

Virgo, D., Mysen, B.O., Danckwerth, P., 1983. Redox equilibria and the anionic structure of Na2O.xSiO2-Fe-O melts: Effect of oxygen fugacity. Carnegie Institut. Washington Year Book 82, 305–309.

Wang, Z., Cooney, T.F., Sharma, S.K., 1993. High temperature structural investigation of Na2O 0.5Fe2O3 3SiO2 and Na2O FeO 3SiO2 melts and glasses. Contrib. Mineral. Petrol. 115, 112–122.

Wang, Z., Cooney, T.F., Sharma, S.K., 1995. In situ structural investigation of iron-containing silicate liquids and glasses. Geochim. Cosmochim. Acta 59, 1571–1577. https://doi.org/10.1016/0016-7037(95)00063-6.

Webb, S.L., Murton, B.J., Wheeler, A.J., 2014. Rheology and the Fe3+−chlorine reaction in basaltic melts. Chem. Geol. 366:24–31. https://doi.org/10.1016/j.chemgeo.2013.12.006.

Webster, J.D., Taylor, R.P., Bean, C., 1993. Pre-eruptive melt composition and constraints on degassing of a water-rich pantellerite magma, Fantale volcano, Ethiopia. Contrib. Mineral. Petrol. 114, 53–62.

White, J.C., Parker, D.F., Ren, M., 2009. The origin of trachyte and pantellerite from Pantelleria, Italy: insights from major element, trace element, and thermodynamic modelling. J. Volcanol. Geotherm. Res. 179:33–55. https://doi.org/10.1016/j.jvolgeores.2008.10.007.

Wilke, M., 2005. Fe in magma – An overview. Ann. Geophys. 48.

Xu, H., Lee, S., Xu, H., 2017. Luogufengite: a new nano-mineral of Fe2O3 polymorph with giant coercive field. Am. Mineral. 102:711–719. https://doi.org/10.1007/s11595-013-0806-2.

Zellmer, G.F., Sakamoto, N., Hwang, S.-L., Matsuda, N., Iizuka, Y., Moebis, A., Yurimoto, H., 2016. Inferring the effects of compositional boundary layers on crystal nucleation, growth textures, and mineral chemistry in natural volcanic Tephras through submicron-resolution imaging. Front. Earth Sci. 4:1–7. https://doi.org/10.3389/feart.2016.00088.

Zhang, Y., 1999. A criterion for the fragmentation of bubbly magma based on brittle failure theory. Nature 402, 648–650.